Causes of Enhanced SST Variability over the Equatorial Atlantic and Its Relationship to the Atlantic Zonal Mode in CMIP5

YUN YANG

State Key Laboratory of Earth Surface Processes and Resource Ecology, and College of Global Change and Earth System Science, Beijing Normal University, Beijing, China

SHANG-PING XIE

Scripps Institution of Oceanography, University of California, San Diego, La Jolla, California, and Physical Oceanography Laboratory/CIMST, Ocean University of China, and Qingdao National Laboratory for Marine Science and Technology, Qingdao, China

LIXIN WU

Physical Oceanography Laboratory/CIMST, Ocean University of China, and Qingdao National Laboratory for Marine Science and Technology, Qingdao, China

YU KOSAKA

Research Center for Advanced Science and Technology, University of Tokyo, Tokyo, Japan

JIANPING LI

State Key Laboratory of Earth Surface Processes and Resource Ecology, and College of Global Change and Earth System Science, Beijing Normal University, Beijing, and Laboratory for Regional Oceanography and Numerical Modeling, Qingdao National Laboratory for Marine Science and Technology, Qingdao, China

(Manuscript received 8 December 2016, in final form 8 May 2017)

ABSTRACT

A spurious band of enhanced sea surface temperature (SST) variance (SBEV) is identified over the northern equatorial Atlantic in the Geophysical Fluid Dynamics Laboratory (GFDL) Climate Model, version 2.1. The SBEV is especially pronounced in boreal spring owing to the combined effect of both anomalous atmospheric thermal forcing and oceanic vertical upwelling. The SBEV is a common bias in phase 5 of the Coupled Model Intercomparison Project (CMIP5), found in 14 out of 23 models. The SBEV in CMIP5 is associated with the atmospheric thermal forcing and the oceanic vertical upwelling, similar to GFDL CM2.1. While the tropical North Atlantic variability is only weakly correlated with the Atlantic zonal mode (AZM) in observations, the SBEV in CMIP5 produces conditions that drive and intensify the AZM variability via triggering the Bjerknes feedback. This partially explains why AZM is strong in some CMIP5 models even though the equatorial cold tongue and easterly trades are biased low.

1. Introduction

The tropical Atlantic features prominent interannual variability of sea surface temperature (SST) and exerts a profound influence on rainfall variability over the surrounding continents (Giannini et al. 2003; Xie and Carton 2004), Atlantic hurricane activity (Xie et al. 2005; Vimont 2012), the Indian monsoon (Kucharski et al. 2007), El Niño–Southern Oscillation (ENSO) (Keenlyside et al. 2013; Ham et al. 2013; Yang et al. 2017), and tropical Pacific decadal variability (McGregor et al. 2014; Li et al. 2016). Two modes of SST variability are distinct over the tropical Atlantic (e.g., Xie and Carton 2004). One is the Atlantic zonal mode (AZM), which peaks during boreal

Corresponding author: Yun Yang, yunyang@bnu.edu.cn

DOI: 10.1175/JCLI-D-16-0866.1

TABLE 1. CMIP5 models and members of three ensembles, classified according to the SBEV variability and its relative magnitude to the Dakar Niño. Specifically, Strong SBEV models display the largest SST variance over the SBEV region; Weak SBEV models feature max variance over the Dakar Niño region and a secondary extreme over the SBEV region; and No SBEV models show weak SBEV variance (see Fig. 7). Only one simulation is used for each model and during the period of 1870–2015.

Model	Strong SBEV models	Weak SBEV models	No SBEV models
ACCESS1.0			X
ACCESS1.3			X
BCC_CSM1.1		X	
BCC_CSM1.1(m)		X	
BNU-ESM			X
CCSM4		X	
CESM1(BGC)		X	
CMCC-CESM	X		
CMCC-CM			X
CMCC-CMS		X	
CNRM-CM5			X
FIO-ESM		X	
GFDL CM2.1	X		
GFDL CM3	X		
GFDL-ESM2G		X	
GFDL-ESM2M	X		
INM-CM4.0			X
MIROC5	X		
MPI-ESM-LR			X
MPI-ESM-MR			X
MPI-ESM-P			X
NorESM1-M	X		
NorESM1-ME	X		

summer (Philander 1986; Carton and Huang 1994; Davey et al. 2002; Xie and Carton 2004). This mode is thought to be governed by the Bjerknes feedback (Bjerknes 1969), the dynamics responsible for ENSO in the tropical Pacific (Zebiak 1993; Keenlyside and Latif 2007; Ding et al. 2010). Another mode is the Atlantic meridional mode (AMM), phase locked in boreal spring. Studies have attributed the development of the AMM to the wind–evaporation–SST (WES) feedback (Xie and Philander 1994; Chang et al. 1997).

General circulation models (GCMs) suffer from severe biases in simulating tropical Atlantic climate. Atmospheric and coupled GCMs simulate a double intertropical convergence zone (ITCZ) in spring. In observations, the ITCZ is located in the Northern Hemisphere throughout the year (e.g., Xie and Philander 1994). The ITCZ in CMIP5, however, has a spurious band in the Southern Hemisphere, due to the biased maximum SST (Stockdale et al. 2006; Doi et al. 2010; Yang et al. 2017). Another prominent bias is a reversed SST gradient over the equator in boreal summer, with the eastern basin warmer than the western basin. This bias has not been improved significantly in models from phase 5 of the Coupled Model Intercomparison Project (CMIP5) (Richter et al. 2014). The reversed gradient is closely related to the westerly wind stress bias in boreal spring, originating in both land surface processes and the latitudinal position of the ITCZ (Chang et al. 2007; Richter and Xie 2008; Tozuka et al. 2011; Richter et al. 2012, 2014). By deepening the thermocline in the east, the westerly biases would lead to failure in reproducing cold tongue development in boreal summer (Davey et al. 2002; Richter and Xie 2008), from which we would expect a reduced AZM variability. Some CMIP5 models, however, display equivalent or even overestimated AZM variability (Richter et al. 2014). This indicates that some other factors might help to enhance the AZM variability.

In this study, we find that a spurious band of enhanced SST variance (SBEV) north of the equator in boreal spring is a common bias among CMIP5 models. The SBEV in CMIP5 produces conditions that trigger the Bjerknes feedback, which then drives and intensifies the AZM variability in boreal summer.

This study is organized as follows. Section 2 gives a brief introduction of data used in this study. Section 3 introduces the SBEV bias in a single model and thoroughly analyzes the characteristics and mechanisms of this bias. The Geophysical Fluid Dynamics Laboratory (GFDL) Climate Model, version 2.1, is chosen for the thorough investigation, in which the strongest SBEV

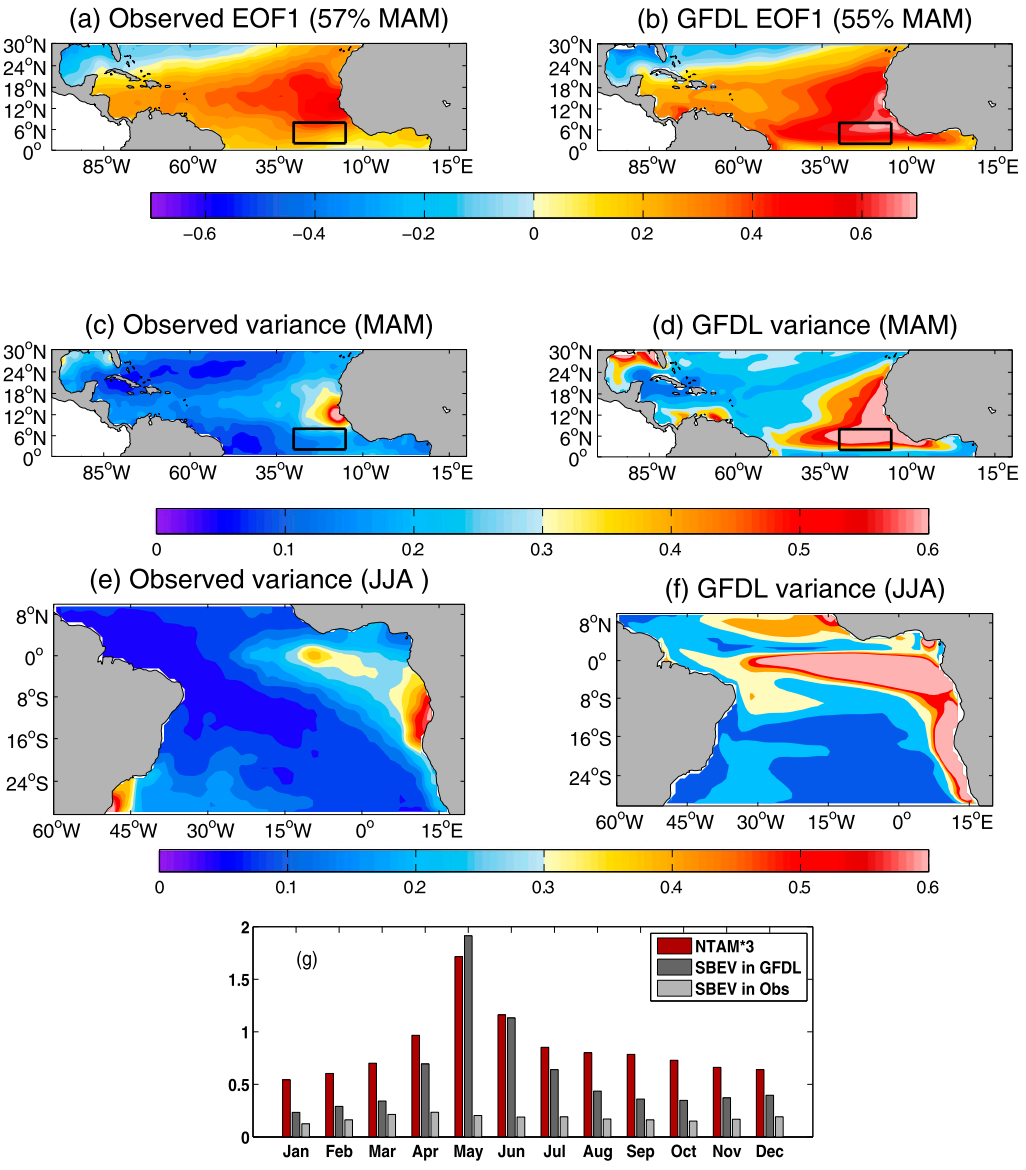

FIG. 1. (a),(b) First EOF mode of SST (°C) over 0°–30°N, 100°W–20°E during MAM; (c),(d) SST variance (°C^2) in MAM; and (e),(f) SST variance (°C^2) in JJA, for (left) observed and (right) GFDL CM2.1 data. The black box in (a)–(d) represents the domain of the SBEV (2°–8°N, 30°–15°W). (g) Variance (°C^2) of the SBEV in GFDL CM2.1, the SBEV in observations, and NTAM (defined as SST averaged over 0°–25°N, 60°W–0°) in GFDL CM2.1 as a function of calendar months.

variability among CMIP5 is identified. Section 4 studies the SBEV in CMIP5 and its connection with the AZM. The paper finally concludes with a summary and discussion in session 5.

2. CMIP5 and observational datasets

In this study, we analyze historical output from GFDL CM2.1 (Delworth et al. 2006), during 1870–2015. The data are based on historical output and extended with RCP4.5. The atmospheric component is based on the GFDL Atmospheric Model, version 2.1 (AM2.1), with a resolution of 2.5° longitude × 2.0° latitude and 24 vertical levels (Anderson et al. 2004). The oceanic component is the Modular Ocean Model (MOM), version 4 (Griffies et al. 2003), with 50 vertical layers. The horizontal resolution is 1.0° longitude × 1.0° latitude over the extratropics and increases to 1.0° longitude × ⅓° latitude between 30°S and 30°N.

We also use historical integrations from CMIP5 models. Table 1 lists 23 models used in this study and the members of the three groups. We classify the models according to the displayed SBEV variability and its relative magnitude to the Dakar Niño. The Dakar Niño is the center of maximum variability off the coast of Senegal [see a recent paper by Oettli et al. (2016)]. Models that display the largest SST variance in the SBEV region are classified as Strong SBEV; models that place the maximum SST variance over the Dakar Niño are classified as Weak SBEV; and models in a third group, No SBEV, display only weak SST variance in the SBEV region as the observations (Fig. 7).

Model output is compared to the observation and reanalysis data. The monthly mean SST data are taken from the Hadley Centre Sea Ice and Sea Surface Temperature dataset (HadISST; Rayner et al. 2003), from 1870 to 2015. Surface wind and wind stress are taken from the European Centre for Medium-Range Weather Forecasts (ECMWF) interim reanalysis (ERA-Interim), during 1979–2015 (Dee et al. 2011). Precipitation, during the period of 1979–2015, is from the Global Precipitation Climatology Project (GPCP; Adler et al. 2003). All the observed and CMIP5 (including GFDL CM2.1) model data are detrended to remove the long-term warming trend.

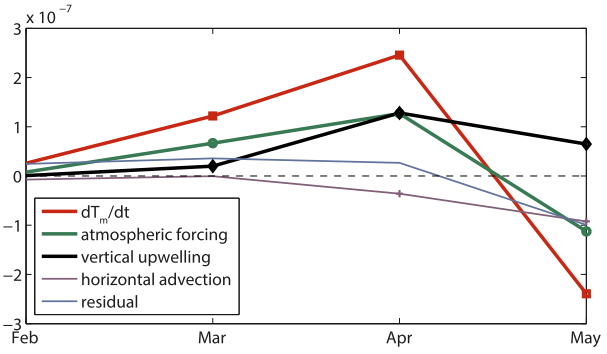

FIG. 2. Lagged regression of individual heat budget terms against the SBEV index (°C s^{-1}) in May, based on GFDL CM2.1. Only points passing the 95% significance level are marked.

In boreal spring, the dominant SST variability over the north tropical Atlantic (NTA) is the north tropical

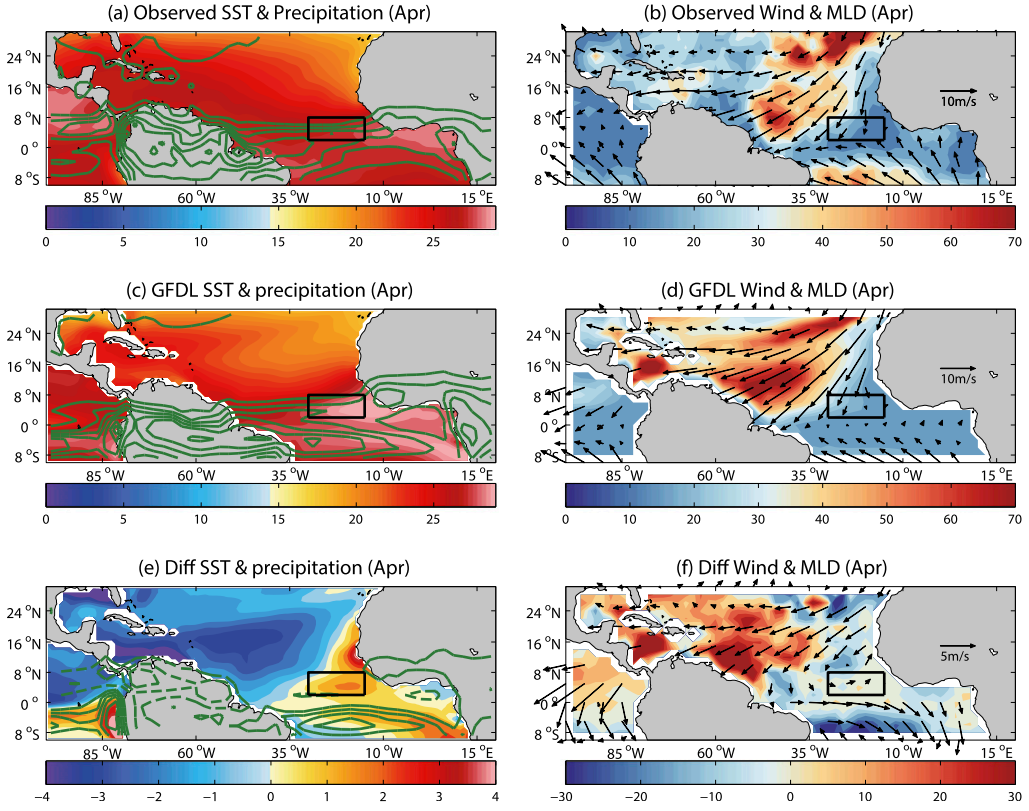

FIG. 3. Climatological mean state of (left) SST (°C; color shading) and precipitation (mm day^{-1}; contours with interval at 2 mm day^{-1}), and (right) MLD (m; color shading) and surface wind velocity (m s^{-1}; vector) in April, in from (a),(b) observations; (c),(d) GFDL CM2.1; and (e),(f) their differences (GFDL CM2.1 minus observations). The black box represents the domain of the SBEV.

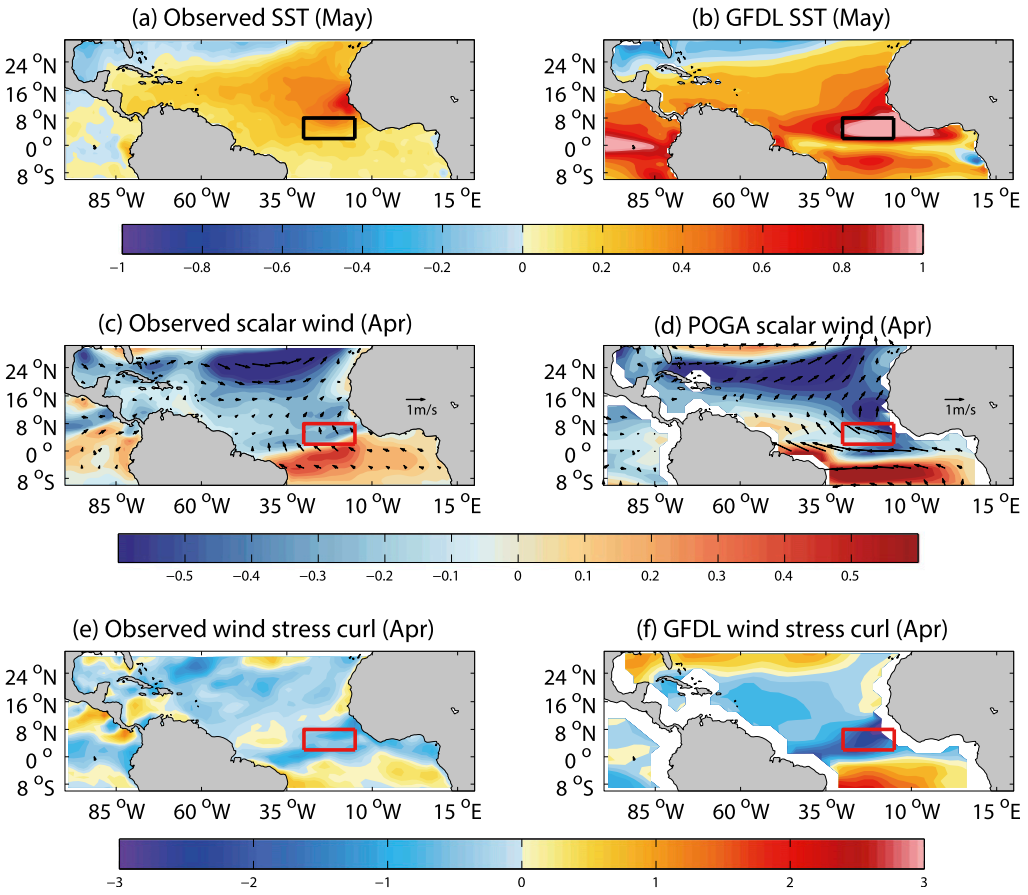

FIG. 4. Regressed anomalies of (a),(b) SST (°C) in May; (c),(d) surface scalar wind speed ($m\,s^{-1}$, color shading) and surface wind velocity (vector) in April; and (e),(f) wind stress curl ($10^{-8}\,N\,m^{-3}$) in April against the SBEV index in May, using the (left) observed and (right) GFDL CM2.1 data. The box represents the domain of the SBEV.

Atlantic mode (NTAM; Fig. 1a), also known as the northern pole of the AMM (e.g., Wu et al. 2004; Yang et al. 2017). In GFDL CM2.1, the NTAM also emerges as the leading empirical orthogonal function mode (EOF1) of MAM SST (Fig. 1b). Biases, however, are apparent. The observed NTAM exhibits maximum anomalies centered off the coast of Senegal; this variability is also known as the Dakar Niño (Oettli et al. 2016). The variability of the Dakar Niño is around 0.6°C in observations and over 0.7°C in GFDL CM2.1. In addition to this center, the model shows an extra extreme variability, exhibiting a narrow band north of the equator (black box in Fig. 1). We call this spurious band of enhanced SST variability the SBEV, and define it as SST averaged over the band 2°–8°N, 30°–15°W. The SBEV bias also stands out in SST variance (cf. Figs. 1c and 1d). The observed SBEV shows weak seasonality and variability (Fig. 1g). In GFDL CM2.1, however, the SBEV is active in boreal spring and peaks in May, consistent with the NTAM. The correlation between the SBEV and the NTAM in May is 0.91 in GFDL CM2.1, indicating that the SBEV represents bias in simulation of the NTAM.

3. Mechanisms of the SBEV

To demonstrate how the SBEV is generated, the mixed layer heat budget analysis is conducted according to

$$\frac{\partial T_m}{\partial t} = \frac{Q - q_{sw}}{\rho C_p H_m} - W\frac{T_m - T_b}{H_m} - U\nabla T_m + \text{residual},$$

where T_m is the mixed layer temperature, which is a proxy of SST. Also, ∂T_m is the change of mixed layer temperature; t is time; ρ and C_p are the density and heat capacity of seawater, respectively; Q is the net surface heat flux into the ocean; q_{sw} is the downward solar

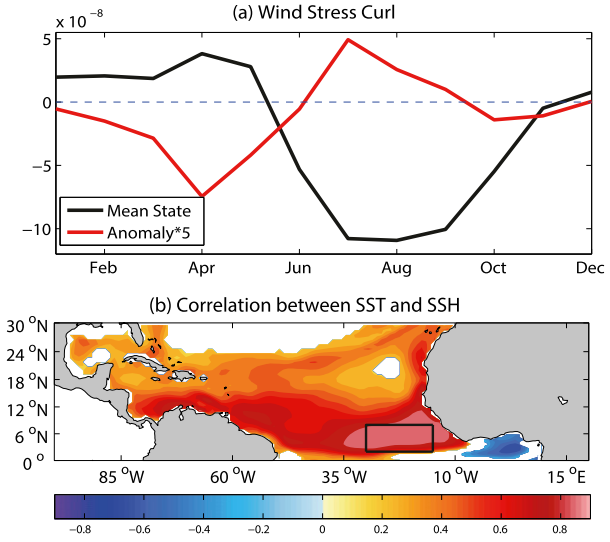

FIG. 5. (a) Regressed anomaly (red) of wind stress curl (N m^{-3}) over the band against the SBEV index in each calendar month. Black curve indicates the corresponding climatology. (b) Local interannual correlation between SST and SSH in May (only showing values passing the 99% significance level). The black box represents the domain of the SBEV. Based on GFDL CM2.1.

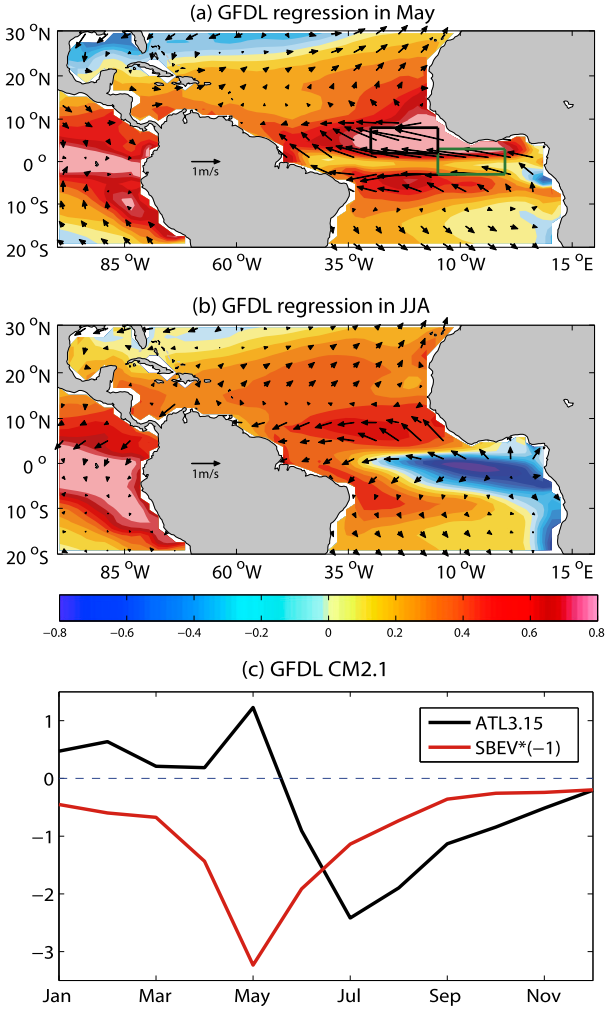

FIG. 6. Regression of SST (°C; color shading) and surface wind velocity (m s^{-1}; vector) in (a) May and (b) JJA onto the SBEV index in May, based on GFDL CM2.1. The black and green boxes in (a) represent the SBEV and ATL3.15 region, respectively. (c) Time series (°C) of composite anomalies of the SBEV (reversed sign) and ATL3.15 indices for warm (above one std dev) minus cold (below one std dev) SBEV events.

insolation penetrating through the bottom of the mixed layer; H_m is the mixed layer depth; U and W are the horizontal and vertical velocity, respectively; and T_b is the mixed layer bottom temperature, defined as the temperature 5 m below the mixed layer. The residual contains, among others, turbulent mixing, which we estimate is the dominant contributor for this term. The first term on the right-hand side describes the atmospheric thermal forcing. The second and third terms represent oceanic cooling through vertical and horizontal advection, respectively.

The SBEV variations are primarily associated with atmospheric thermal forcing and oceanic vertical upwelling (Fig. 2). These two terms start to grow in March, peak in April, and quickly decay afterward. This is consistent with the rate of SST change. The contribution of horizontal advection terms, however, is weak in GFDL CM2.1. In the model climatology, the equatorial Atlantic displays warmer SST in the east than in the west, which leads to equatorial westerly bias and a slowdown of the atmospheric circulation (Figs. 3c,d). Such characteristics limit the horizontal advection, similar to previous findings on the climatology, the AZM, Dakar Niño, and South Atlantic Ocean dipole (Richter et al. 2012; Nnamchi et al. 2015, 2016; Oettli et al. 2016). In boreal spring, the mixed layer depth (MLD) is shallow over the band, with an average of 20 m in GFDL CM2.1 (Fig. 3d). Thus SST variability is sensitive to perturbations from the atmosphere and the ocean.

The atmospheric forcing plays an important role in the development of the SBEV. The NTAM grows and penetrates toward the equator with the WES feedback. As the warming reaches the coast of Senegal, it triggers southeasterly anomalies over the band (Fig. 4d). These anomalies weaken the background wind and decrease the evaporation, leading to the warming of SST.

The oceanic process is another key factor. In boreal spring, the climatological wind stress curl is positive over the band (Fig. 5a), in response to the northeasterly trades and equatorial westerlies (Fig. 3d). This positive wind stress curl favors Ekman upwelling in the mean state, consistent with the shallow thermocline (not shown). In response to the warming of SBEV, the

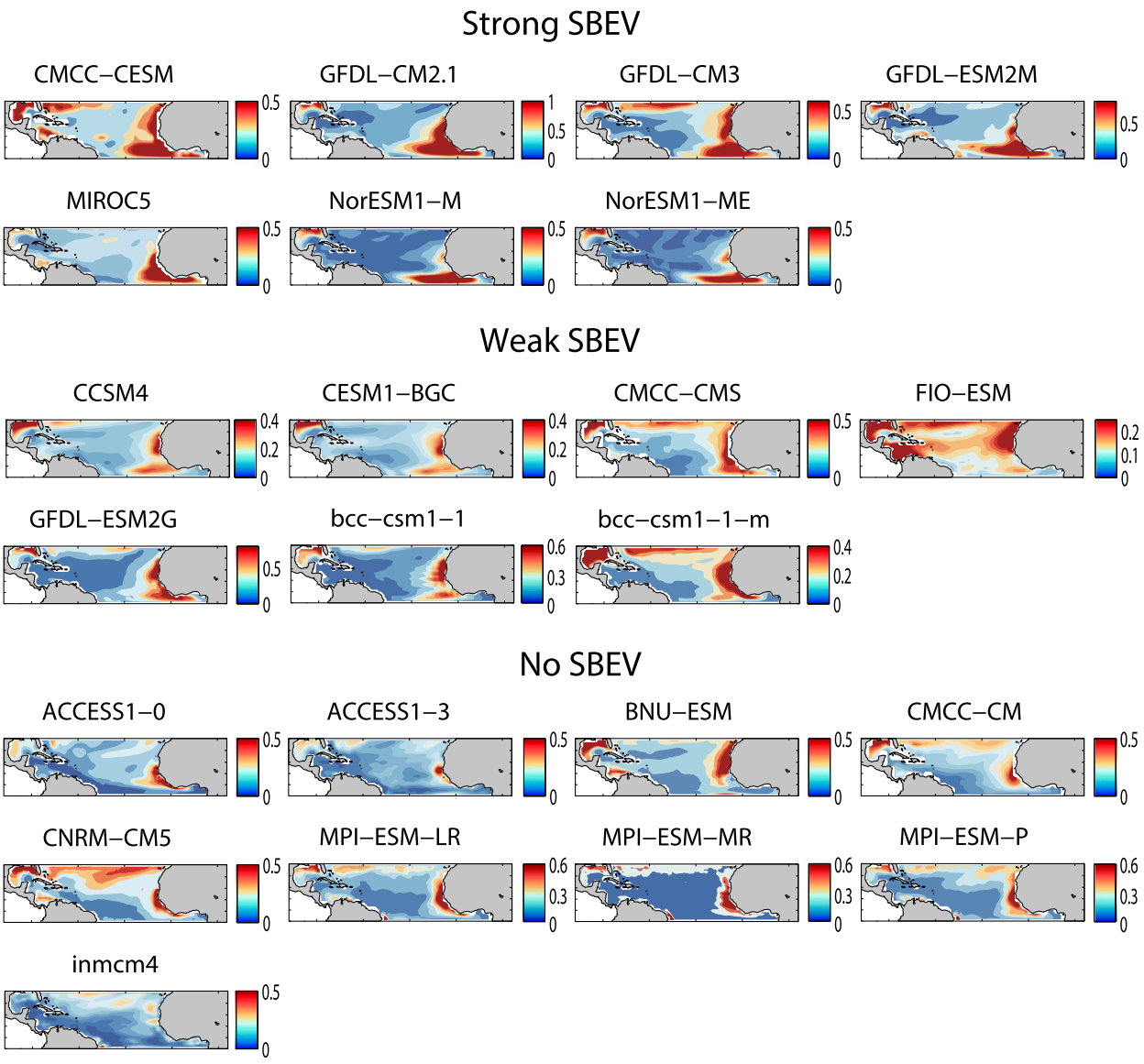

FIG. 7. SST interannual variance ($°C^2$) in May in CMIP5 models.

strong equatorial easterly anomalies generate remarkable wind shear over the band (Fig. 4d). The associated negative wind stress curl anomalies (Fig. 5a) force the anomalous Ekman downwelling, which suppresses cold water upwelling from the subsurface in climatology and warms the SST. The tight correlation of sea surface height (SSH) and SST further indicates a robust oceanic process over the SBEV region (Fig. 5b). The correlation is relatively low over the subtropics, supporting that the NTAM is primarily thermodynamically driven (Chang et al. 1997; Amaya et al. 2017).

To have a better understanding of the SBEV, we compare the mechanisms in GFDL CM2.1 to that in observations. The SBEV, featuring a narrow band north of the equator, displays extreme warming in GFDL CM2.1 but weak variations in observations (Figs. 4a,b). These features cannot be explained by the atmospheric forcing that displays a decrease in wind speed over the entire NTA for both observations and GFDL CM2.1 (Figs. 4c,d). The distinct oceanic vertical upwelling anomalies, however, are restrained to the SBEV region and barely observed in the physical world (Figs. 4e,f). Involving this oceanic process makes the SBEV an extreme SST variance center and a unique variability. The MLD bias (1.5 m) is insufficient to generate this distinct difference in vertical advection term between GFDL CM2.1 and observations.

Another interesting issue, compared to the observations, is the southward extension of reduced wind speed in GFDL CM2.1 (Fig. 4). According to Zhang et al. (2014b), the equatorward extension of NTAM is supported by the WES feedback and unable to penetrate beyond the latitude of ITCZ where wind converges. The observed wind converges to the south of the band in April (Fig. 3b), consistent with the boundary of the decreased wind speed (Fig. 4c). The biased double ITCZ in our model, in contrast, shifts the wind convergence zone southward (Fig. 3c) as in other CMIP5 models. The corresponding decrease in wind speed penetrates to the equator, acting to warm the local SST (Fig. 4d). This warming effect, however, is suppressed by the anomalous upwelling associated with the equatorial easterly anomalies.

The SBEV in boreal spring is accompanied by strong equatorial easterly anomalies (Fig. 6a), which drives AZM events in the following summer via triggering the Bjerknes feedback (Fig. 6b). Composite analysis is performed to study the evolution of the SBEV and AZM (Fig. 6c). We use the ATL3.15 index, defined as SST averaged over 3°S–3°N and 15°–0°W, to represent the AZM. The SBEV starts to grow in March and peaks in May. The ATL3.15 also warms up in boreal spring, due to the decrease in wind speed (Fig. 4d). After that, it cools rapidly and reaches its mature phase in July, two months later than the SBEV. The correlation coefficient is largest when SBEV leads ATL3.15 by two months ($r = -0.67$, passing the 99% significance level). Moreover, the AZM in GFDL CM2.1 displays much stronger variability than the observations, with June–August (JJA) ATL3.15 variance of 1.13°C^2 and 0.27°C^2, respectively (Figs. 1e,f). This difference might be partially attributed to the SBEV influence.

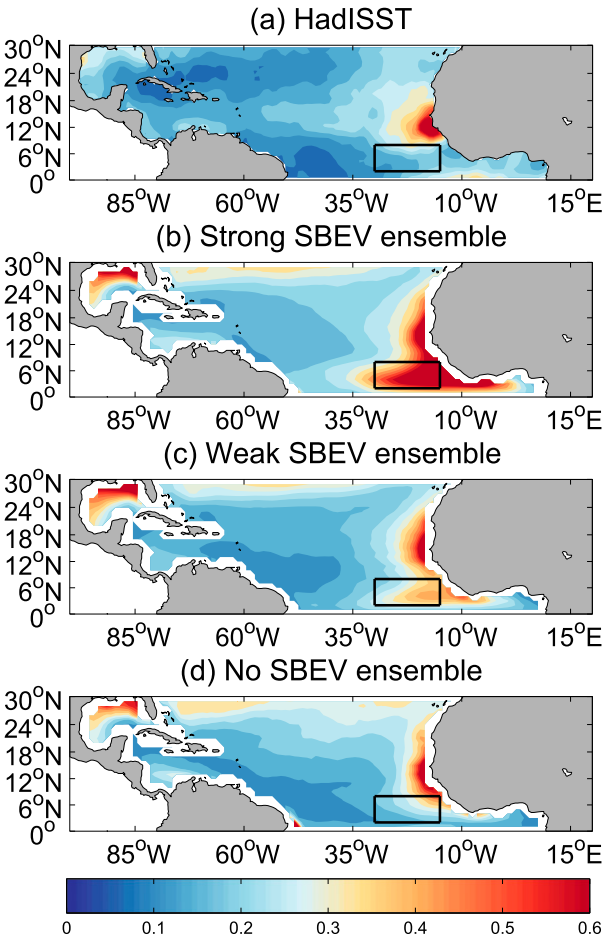

FIG. 8. Interannual variance of May SST (°C^2) in the (a) observations, and ensembles of (b) Strong, (c) Weak, and (d) No SBEV.

4. The SBEV in CMIP5

We assess the SBEV existence in CMIP5 models by calculating SST variance in May, when its variability peaks among most models (not shown). It is found that 14 out of 23 models display spurious strong variance over the band (Fig. 7), indicating that the SBEV is a common bias among CMIP5 models. We classify the CMIP5 models into three groups: Strong SBEV, Weak SBEV, and No SBEV (Table 1). The ensembles of SST variance in different groups are shown in Fig. 8. The No SBEV group displays weak variance over the SBEV region, consistent with the observations. Although the other two ensembles both feature robust SBEV variability, differences are apparent. The maximum SST variance is located over the SBEV region for the Strong SBEV ensemble while over the Dakar Niño in the Weak SBEV ensemble.

As in GFDL CM2.1, the atmospheric forcing and oceanic vertical upwelling are both responsible for the evolution of SBEV in CMIP5. All models reveal a decrease of wind speed associated with the warming of SBEV (not shown). This warming is further enhanced by the anomalous oceanic downwelling associated with wind stress curl anomalies (Fig. 9a).

The difference in SBEV magnitude among three groups is primarily attributed to the different intensity of oceanic vertical upwelling rather than of atmospheric forcing. Specifically, the ranges of correlation coefficients between the SBEV and wind speed are similar among three ensembles (not shown). However, the oceanic process is most (least) prominent among the Strong SBEV (No SBEV) models, corresponding to the tightest (loosest) connection between the SBEV and Ekman pumping (Fig. 9a) and strongest (weakest) ensemble of wind stress curl anomalies (Fig. 10).

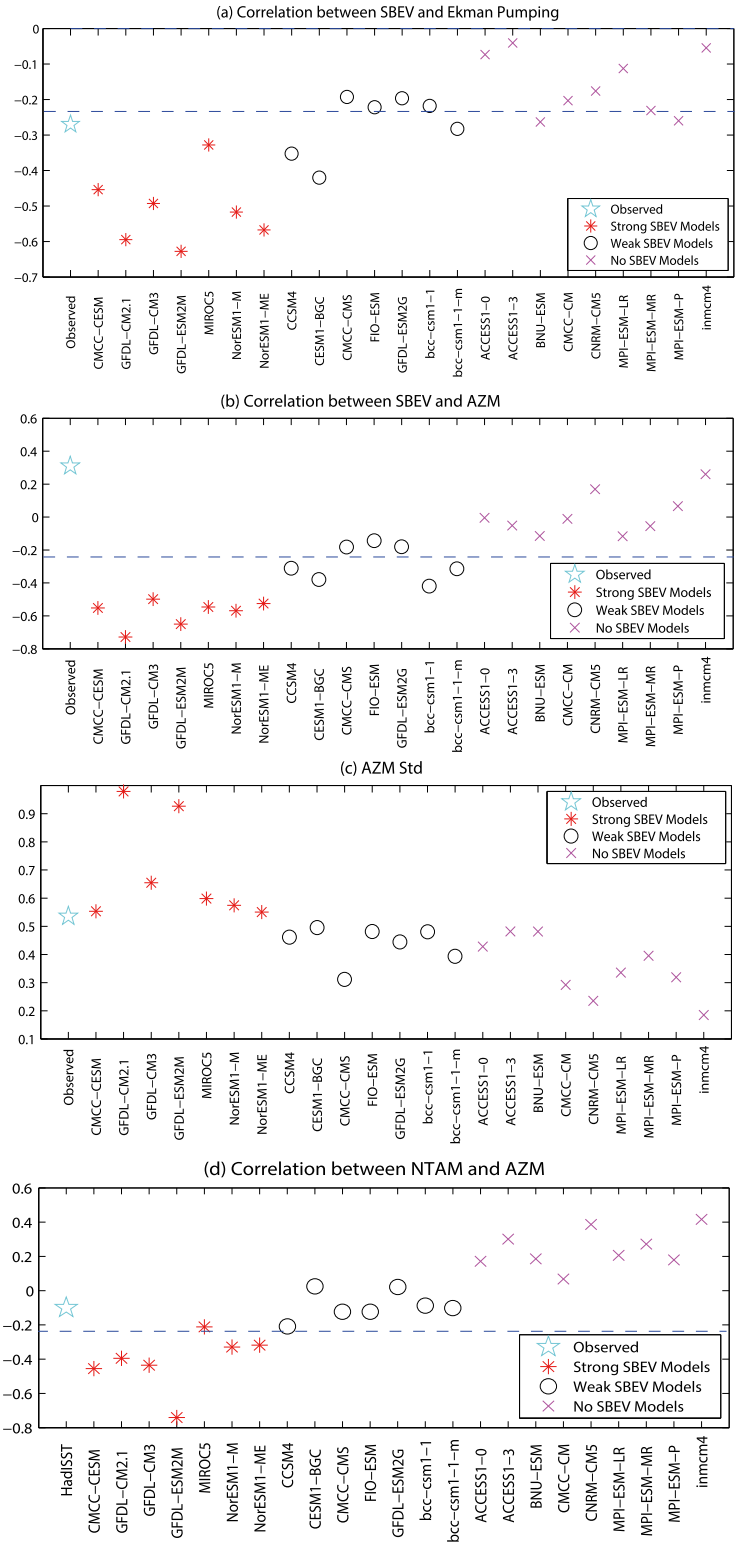

FIG. 9. Correlation of the SBEV index in May with (a) wind stress curl in April and (b) ATL3.15 SST in JJA. (c) Std dev of ATL3.15 SST in JJA (°C). (d) Correlation of NTAM in May and ATL3.15 SST in JJA. Blue dotted lines represent 99% significance level.

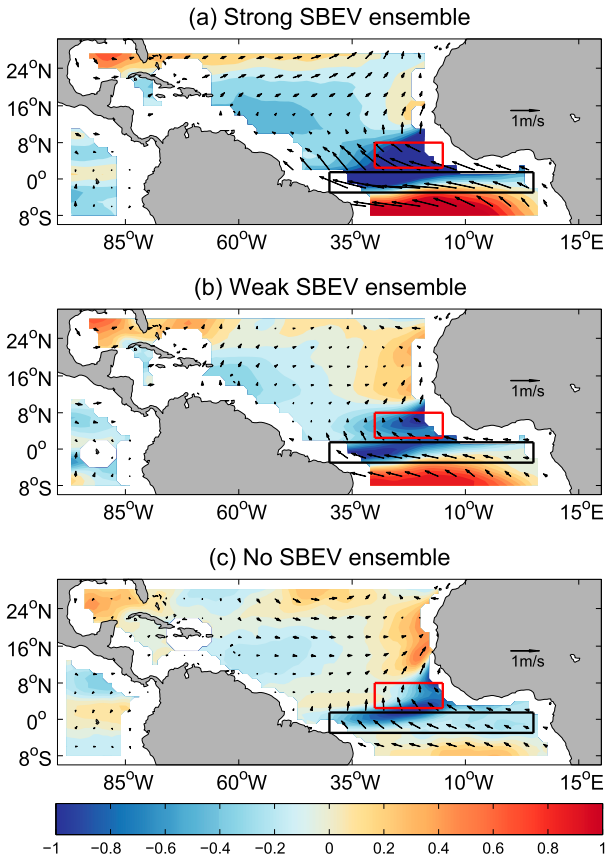

FIG. 10. Regression of April wind stress curl (10^{-8} N m^{-3}; color shading) and wind (m s^{-1}; vector) anomalies onto the SBEV index in May in different ensembles.

The SBEV bias enhances AZM variability in CMIP5. In boreal spring, most CMIP5 models display biased equatorial westerlies (e.g., Richter et al. 2014). This wind bias would deepen the thermocline in the east and prevent the cold tongue development, from which we would expect a weaker AZM variability in CMIP5 than in observations. However, most Strong and Weak SBEV models display overestimated or equivalent AZM variability (Fig. 9c). The ensemble with stronger SBEV displays more intensified AZM variability (Fig. 11). The AZM in the Strong SBEV ensemble, with a variance of 0.51°C^2, surpasses the observations (0.27°C^2) and features 4 times the variance of the No SBEV ensemble. Moreover, the connection between the SBEV and the AZM is closest among the Strong SBEV, in which a maximum (averaged) correlation coefficient reaches −0.75 (−0.58, Fig. 9b). The difference of this connection originates from the equatorial wind anomalies in response to the SBEV (Fig. 10). The Strong and Weak SBEV ensembles display anomalous equatorial easterlies in boreal spring, which would trigger the AZM events in the following summer via the Bjerknes feedback. The wind anomalies are larger in the Strong SBEV, consistent with the more intensified AZM variability. The No SBEV ensemble displays southeasterly anomalies over the equator, which is not helpful in enhancing the AZM variability.

5. Summary and discussion

In GFDL CM2.1, the NTAM in spring shows two centers of maximum variability. One is the Dakar Niño as in observations. The other one is the SBEV bias, featuring a narrow band located north of the equator. The SBEV is phase locked in spring, in accordance with the NTAM. The development of the SBEV is attributed to both the atmospheric thermal forcing and oceanic vertical upwelling. The wind anomalies warm the SST by weakening the background wind. The anomalous Ekman downwelling associated with wind stress curl anomalies further enhances this warming by suppressing the climatological Ekman upwelling. Moreover, the shallow mixed layer over the SBEV region makes the SST sensitive to perturbations from the atmosphere and the ocean. The SBEV in spring can drive AZM events in summer via triggering the Bjerknes feedback. The AZM in GFDL CM2.1 displays larger variability than in observations, even with a reduced cold tongue development.

The SBEV is a common bias among CGCMs, existing in 14 out of 23 CMIP5 models. The mechanisms of the SBEV in CMIP5 involve the atmospheric forcing and oceanic vertical upwelling, similar to GFDL CM2.1. Models with stronger SBEV display more intensified AZM variability, due to the important role of the SBEV in driving the AZM events.

The SBEV enhances the interaction between the extratropical North Atlantic and equatorial Atlantic. Previous studies suggest a fragile relationship between the NTAM and AZM (Foltz and McPhaden 2010). Similar results are found in the Pacific Ocean (Clement et al. 2011; Zhang et al. 2014a). Using an idealized model, Zhang et al. (2014b) indicate that the ITCZ, located in the Northern Hemisphere, prevents the extratropical signal in the North Pacific from reaching the equator. However, the biased double ITCZ in CMIP5 allows the NTAM-related SST anomalies to propagate to the SBEV region with WES feedback, which would further trigger AZM events in summer. The correlation between NTAM and AZM in the Strong SBEV is much higher than that in observations (Fig. 9d).

In this paper, historical integrations in CMIP5 are used to compare with the observations. The strong SBEV bias also exists in preindustrial outputs (not shown). Moreover, we emphasize the SBEV effect on

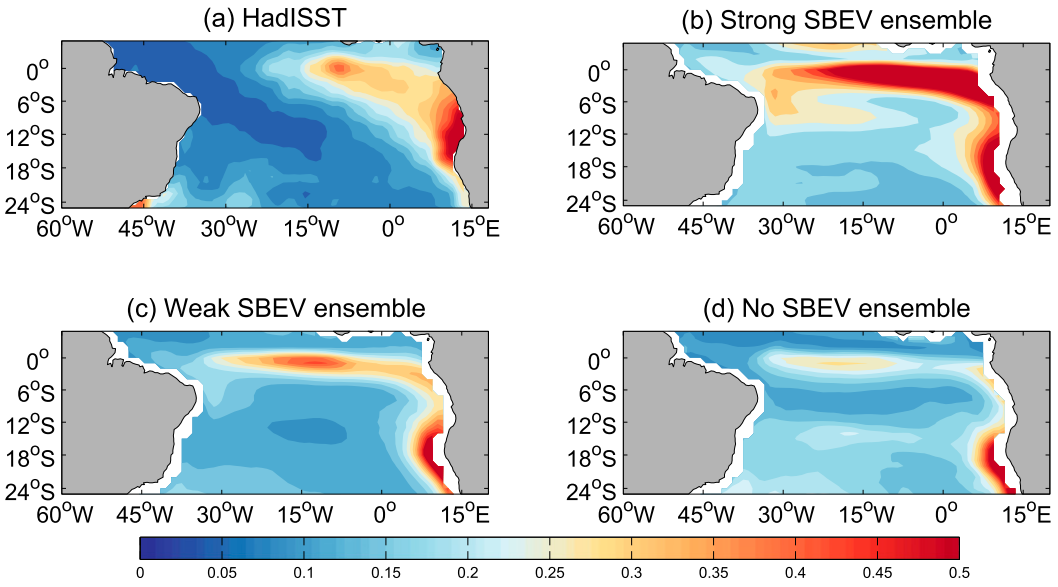

FIG. 11. Interannual variance of JJA SST ($°C^2$) in the (a) observations, and ensembles of (b) Strong, (c) Weak, and (d) No SBEV.

AZM variability via triggering the Bjerknes feedback. Recent studies suggest that meridional advection (Richter et al. 2013) and thermodynamic feedback (Nnamchi et al. 2015) also contribute to the development of AZM. These mechanisms are beyond the scope of this study and will not be discussed in this paper.

Acknowledgments. The authors wish to thank the anonymous reviewers for their constructive comments that helped to improve this paper. This work is supported by the National Science Foundation of China (41606008 and 41521091), the National Basic Research Program of China (2012CB955600), the NOAA Climate Program Office (NA13OAR4310092), Climate Change Special Fund (2016YFA0601803), the Postdoctoral Science Foundation of China (2015M581016), and the Fundamental Research Funds for the Central Universities (2015NT07). YK is supported by the Japan Society for the Promotion of Science through Grant-in-Aid for Young Scientists (A) 15H05466 and the Japan Science and Technology Agency through Belmont Forum CRA "InterDec."

REFERENCES

Adler, R. F., and Coauthors, 2003: The version-2 Global Precipitation Climatology Project (GPCP) monthly precipitation analysis (1979–present). *J. Hydrometeor.*, **4**, 1147–1167, doi:10.1175/1525-7541(2003)004<1147:TVGPCP>2.0.CO;2.

Amaya, D. J., M. J. DeFlorio, A. J. Miller, and S.-P. Xie, 2017: WES feedback and the Atlantic meridional mode: Observations and CMIP5 comparisons. *Climate Dyn.*, doi:10.1007/s00382-016-3411-1, in press.

Anderson, J. L., and Coauthors, 2004: The new GFDL global atmosphere and land model AM2/LM2: Evaluation with prescribed SST simulations. *J. Climate*, **17**, 4641–4673, doi:10.1175/JCLI-3223.1.

Bjerknes, J., 1969: Atmospheric teleconnections from the equatorial Pacific. *Mon. Wea. Rev.*, **97**, 163–172, doi:10.1175/1520-0493(1969)097<0163:ATFTEP>2.3.CO;2.

Carton, J. A., and B. Huang, 1994: Warm events in the tropical Atlantic. *J. Phys. Oceanogr.*, **24**, 888–903, doi:10.1175/1520-0485(1994)024<0888:WEITTA>2.0.CO;2.

Chang, C.-Y., J. A. Carton, S. A. Grodsky, and S. Nigam, 2007: Seasonal climate of the tropical Atlantic sector in the NCAR Community Climate System Model 3: Error structure and probable causes of errors. *J. Climate*, **20**, 1053–1070, doi:10.1175/JCLI4047.1.

Chang, P., L. Ji, and H. Li, 1997: A decadal climate variation in the tropical Atlantic Ocean from thermodynamic air–sea interactions. *Nature*, **385**, 516–518, doi:10.1038/385516a0.

Clement, A. C., P. DiNezio, and C. Deser, 2011: Rethinking the ocean's role in the Southern Oscillation. *J. Climate*, **24**, 4056–4072, doi:10.1175/2011JCLI3973.1.

Davey, M. K., and Coauthors, 2002: STOIC: A study of coupled model climatology and variability in tropical ocean regions. *Climate Dyn.*, **18**, 403–420, doi:10.1007/s00382-001-0188-6.

Dee, D. P., and Coauthors, 2011: The ERA-Interim reanalysis: Configuration and performance of the data assimilation systems. *Quart. J. Roy. Meteor. Soc.*, **137**, 553–597, doi:10.1002/qj.828.

Delworth, T. L., and Coauthors, 2006: GFDL's CM2 global coupled climate models. Part I: Formulation and simulation characteristics. *J. Climate*, **19**, 643–674, doi:10.1175/JCLI3629.1.

Ding, H., N. S. Keenlyside, and M. Latif, 2010: Equatorial Atlantic interannual variability: The role of heat content. *J. Geophys. Res.*, **115**, C09020, doi:10.1029/2010JC006304.

Doi, T., T. Tozuka, and T. Yamagata, 2010: The Atlantic meridional mode and its coupled variability with the Guinea Dome. *J. Climate*, **23**, 455–475, doi:10.1175/2009JCLI3198.1.

Foltz, G. R., and M. J. McPhaden, 2010: Interaction between the Atlantic meridional and Niño modes. *Geophys. Res. Lett.*, **37**, L18604, doi:10.1029/2010GL044001.

Giannini, A., R. Saravanan, and P. Chang, 2003: Oceanic forcing of Sahel rainfall on interannual to interdecadal time scales. *Science*, **302**, 1027–1030, doi:10.1126/science.1089357.

Griffies, S., M. J. Harrison, R. C. Pacanowski, and A. Rosati, 2003: A technical guide to MOM4. GFDL Ocean Group Tech. Rep. 5, NOAA/Geophysical Fluid Dynamics Laboratory, 295 pp.

Ham, Y.-G., J.-S. Kug, J.-Y. Park, and F.-F. Jin, 2013: Sea surface temperature in the north tropical Atlantic as a trigger for El Niño/Southern Oscillation events. *Nat. Geosci.*, **6**, 112–116, doi:10.1038/ngeo1686.

Keenlyside, N. S., and M. Latif, 2007: Understanding equatorial Atlantic interannual variability. *J. Climate*, **20**, 131–142, doi:10.1175/JCLI3992.1.

——, H. Ding, and M. Latif, 2013: Potential of equatorial Atlantic variability to enhance El Niño prediction. *Geophys. Res. Lett.*, **40**, 2278–2283, doi:10.1002/grl.50362.

Kucharski, F., A. Bracco, J. H. Yoo, and F. Molteni, 2007: Low-frequency variability of the Indian monsoon–ENSO relationship and the tropical Atlantic: The ''weakening'' of the 1980s and 1990s. *J. Climate*, **20**, 4255–4266, doi:10.1175/JCLI4254.1.

Li, X., S.-P. Xie, S. T. Gille, and C. Yoo, 2016: Atlantic-induced pan-tropical climate change over the past three decades. *Nat. Climate Change*, **6**, 275–279, doi:10.1038/nclimate2840.

McGregor, S., A. Timmermann, M. F. Stuecker, M. H. England, M. Merrifield, F.-F. Jin, and Y. Chikamoto, 2014: Recent Walker circulation strengthening and Pacific cooling amplified by Atlantic warming. *Nat. Climate Change*, **4**, 888–892, doi:10.1038/nclimate2330.

Nnamchi, H. C., J. Li, F. Kucharski, I.-S. Kang, N. S. Keenlyside, P. Chang, and R. Farneti, 2015: Thermodynamic controls of the Atlantic Niño. *Nat. Commun.*, **6**, 8895, doi:10.1038/ncomms9895.

——, ——, ——, ——, ——, ——, and ——, 2016: An equatorial–extratropical dipole structure of the Atlantic Niño. *J. Climate*, **29**, 7295–7311, doi:10.1175/JCLI-D-15-0894.1.

Oettli, P., Y. Morioka, and T. Yamagata, 2016: A regional climate mode discovered in the North Atlantic: Dakar Niño/Niña. *Sci. Rep.*, **6**, 18782, doi:10.1038/srep18782.

Philander, S. G. H., 1986: Unusual conditions in the tropical Atlantic Ocean in 1984. *Nature*, **322**, 236–238, doi:10.1038/322236a0.

Rayner, N. A., D. E. Parker, E. B. Horton, C. K. Folland, L. V. Alexander, D. P. Rowell, E. C. Kent, and A. Kaplan, 2003: Global analyses of sea surface temperature, sea ice, and night marine air temperature since the late nineteenth century. *J. Geophys. Res.*, **108**, 4407, doi:10.1029/2002JD002670.

Richter, I., and S.-P. Xie, 2008: On the origin of equatorial Atlantic biases in coupled general circulation models. *Climate Dyn.*, **31**, 587–598, doi:10.1007/s00382-008-0364-z.

——, ——, A. T. Wittenberg, and Y. Masumoto, 2012: Tropical Atlantic biases and their relation to surface wind stress and terrestrial precipitation. *Climate Dyn.*, **38**, 985–1001, doi:10.1007/s00382-011-1038-9.

——, S. K. Behera, Y. Masumoto, B. Taguchi, H. Sasaki, and T. Yamagata, 2013: Multiple causes of interannual sea surface temperature variability in the equatorial Atlantic Ocean. *Nat. Geosci.*, **6**, 43–47, doi:10.1038/ngeo1660.

——, S.-P. Xie, S. Behera, T. Doi, and Y. Masumoto, 2014: Equatorial Atlantic variability and its relation to mean state biases in CMIP5. *Climate Dyn.*, **42**, 171–188, doi:10.1007/s00382-012-1624-5.

Stockdale, T. N., M. A. Balmaseda, and A. Vidard, 2006: Tropical Atlantic SST prediction with coupled ocean–atmosphere GCMs. *J. Climate*, **19**, 6047–6061, doi:10.1175/JCLI3947.1.

Tozuka, T., T. Doi, T. Miyasaka, N. Keenlyside, and T. Yamagata, 2011: Key factors in simulating the equatorial Atlantic zonal sea surface temperature gradient in a coupled general circulation model. *J. Geophys. Res.*, **116**, C06010, doi:10.1029/2010JC006717.

Vimont, D. J., 2012: Analysis of the Atlantic meridional mode using linear inverse modeling: Seasonality and regional influences. *J. Climate*, **25**, 1194–1212, doi:10.1175/JCLI-D-11-00012.1.

Wu, L., Q. Zhang, and Z. Liu, 2004: Toward understanding the tropical Atlantic variability using coupled modeling surgery. *Earth Climate: The Ocean–Atmosphere Interaction*, *Geophys. Monogr.*, Vol. 147, Amer. Geophys. Union, 157–170.

Xie, L., T. Yan, L. J. Pietrafesa, J. M. Morrison, and T. Karl, 2005: Climatology and interannual variability of North Atlantic hurricane tracks. *J. Climate*, **18**, 5370–5381, doi:10.1175/JCLI3560.1.

Xie, S.-P., and S. G. H. Philander, 1994: A coupled ocean–atmosphere model of relevance to the ITCZ in the eastern Pacific. *Tellus*, **46A**, 340–350, doi:10.3402/tellusa.v46i4.15484.

——, and J. A. Carton, 2004: Tropical Atlantic variability: Patterns, mechanisms, and impacts. *Earth's Climate: The Ocean–Atmosphere Interaction*, *Geophys. Monogr.*, Vol. 147, Amer. Geophys. Union, 121–142.

Yang, Y., S.-P. Xie, L. Wu, Y. Kosaka, and J. Li, 2017: ENSO forced and local variability of north tropical Atlantic SST: Model simulations and biases. *Climate Dyn.*, doi:10.1007/s00382-017-3679-9, in press.

Zebiak, S. E., 1993: Air–sea interaction in the equatorial Atlantic region. *J. Climate*, **6**, 1567–1586, doi:10.1175/1520-0442(1993)006<1567:AIITEA>2.0.CO;2.

Zhang, H., A. Clement, and P. DiNezio, 2014a: The South Pacific meridional mode: A mechanism for ENSO-like variability. *J. Climate*, **27**, 769–783, doi:10.1175/JCLI-D-13-00082.1.

——, C. Deser, A. Clement, and R. Tomas, 2014b: Equatorial signatures of the Pacific meridional modes: Dependence on mean climate state. *Geophys. Res. Lett.*, **41**, 568–574, doi:10.1002/2013GL058842.